

Shape of the tip and the formation of sidebranches of xenon dendrites

U. Bisang and J. H. Bilgram

Laboratorium für Festkörperphysik, Eidgenössische Technische Hochschule, CH-8093 Zürich, Switzerland

(Received 10 June 1996)

Experimental studies of the growth of three-dimensional xenon dendrites into a supercooled pure melt are presented. The shape of the dendrite tip and the origin of sidebranching are investigated. It is found that the shape in the tip region is not axisymmetric showing a fourfold symmetry. Four fins grow along the dendrite starting immediately behind the tip. Sidebranches develop at the ridges of these fins. The contour of the fins is not parabolic and can be described in dimensionless units, i.e., measured in units of the tip radius R , by a power law $z = a|x|^\beta$, with $a = 0.58 \pm 0.04$ and $\beta = 1.67 \pm 0.05$, where z is oriented along the growth direction of the dendrite and x is the width of the fins. Selective amplification of thermal noise as well as tip splitting has been discussed in the literature as possible origins of sidebranching. It is found that xenon dendrites grow in a stable mode and do not show any temporal oscillations in either the tip velocity or the curvature of the dendrite tip. Therefore, tip splitting can be excluded as an origin of sidebranching. The distance between the tip and the first sidebranch \bar{z}_{SB} of a dendrite has been determined. \bar{z}_{SB} is used to estimate the noise strength needed to form sidebranches as observed in experiments with xenon dendrites. The experimental results, i.e., β , a , and \bar{z}_{SB} , have been compared with analytical studies [E. Brener and D. Temkin, *Phys. Rev. E* **51**, 351 (1995)]. Quantitative agreement between experiment and theory is found. It is concluded that the formation of sidebranches is initiated by thermal fluctuations. Dendritic structures may be characterized by parameters that describe the “integral” dendrite. The fractal dimension is an example of such an integral parameter. The averaged fractal dimension \bar{d}_f of the contour of a dendrite was determined for various supercoolings in the range of 20 mK $\leq \Delta T \leq 150$ mK. The contour is fractal over a range of more than two orders of magnitude in length scale. The fractal dimension is $\bar{d}_f = 1.42 \pm 0.05$ and does not depend on supercooling. [S1063-651X(96)01011-2]

PACS number(s): 68.70.+w, 64.70.Dv, 81.10.Fq

I. INTRODUCTION

Dendritic growth is one of the most common forms of solidification observed in nature. Dendrites are crystals that develop complex, time-dependent shapes. Snowflakes are well-known examples of dendrites. Dendrites often have “treelike” shapes, as in the case of metal dendrites and of rare gas dendrites. Figure 1 shows the tip area a xenon dendrite, as grown in our experiments. Xenon crystallizes in a fcc structure leading to a nonaxisymmetric dendrite with a fourfold symmetry. Four fins can be seen to grow along the dendrites and the sidebranches develop at the ridges of these fins.

Dendritic solidification is an example for phase transitions at conditions far from equilibrium. Dendritic growth often occurs when a material crystallizes from a supercooled melt or supersaturated solution and the growth is limited by diffusion. For example, dendritic growth is commonly encountered when metals and alloys freeze under small thermal gradients, as occurs in most casting and welding processes. Furthermore, in alloys, the details of the dendritic morphology is directly related to material properties, such as toughness and corrosion behavior. Although the effects of the initial dendritic microstructure can be modified by subsequent heat treatments, the final material properties of alloys are generally sensitive to the details of the original dendritic microstructure. Therefore, the understanding and control of dendritic solidification is of great technological interest.

Dendritic growth is also of theoretical interest as an archetypical example of a pattern forming system, where a complex spatial pattern evolves from initially homogeneous starting conditions. The origin of dendritic shapes and other

nonequilibrium growth patterns has been a long-standing question. Although the relevant differential equations and boundary conditions have been known for a long time, the nonlinearities and instabilities occurring during the solidification process have made it difficult to understand even qualitatively how these shapes arise.

The basic mechanism for the surface instability that leads to the formation of sidebranches is the following. Assuming that diffusion controls the solidification process and the growth rate increases with increasing supercooling. Then the

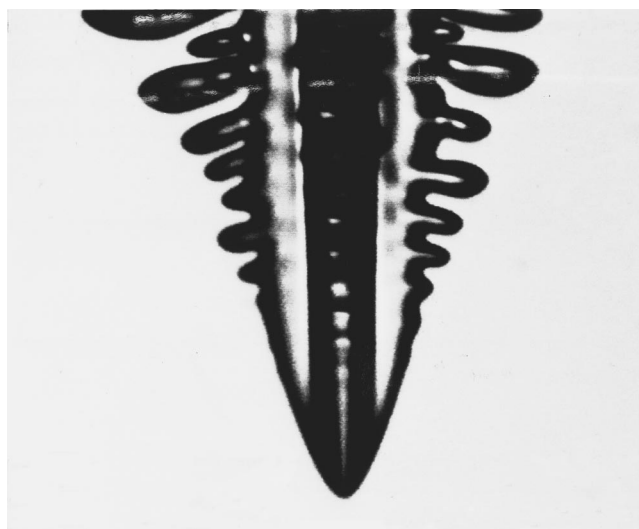


FIG. 1. Xenon dendrite grown at a supercooling of 123 mK. The tip is not axisymmetric and four fins start immediately behind the tip.

crystal grows along the steepest gradient of the diffusion field and forms highly ramified structures.

Ultimately, this morphological instability of the solidification front is limited by capillary forces, and it is the interplay between capillarity and kinetic effects that somehow produces the complex growth patterns that we see in nature. For general reviews about dendrites and solidification see, for example, [1,2]. Even though dendritic growth patterns are due to a morphological interface instability, they are not completely random, showing remarkably regular patterns and deterministic behavior. The big unsolved part of the problem in dendritic solidification is how these regular dendritic patterns are selected. A well-known example for the occurrence of such regular patterns in dendritic growth are snowflakes. Although no two snowflakes look alike, all of them have six regularly spaced sidebranches of equal length.

The so-called velocity-selection problem is an example for the occurrence of deterministic behavior in dendritic growth. Many experiments with various substances were performed [3–5] to measure the tip velocity v_{tip} and the radius of curvature of the tip R of growing dendrites. It was found that v_{tip} and R are uniquely determined by the supercooling or the supersaturation. The question how this unique dynamical operating state of the growing dendrite is selected has been the topic of intensive research during the past years.

Recently, the velocity-selection problem seems to have been solved with the development of microscopic solvability theory. For a review see [6]. But many other questions are still open. The exact shape of the dendrite tip is among the topics under discussion. Most theoretical studies assume that the dendrite tip can be represented by a rotational paraboloid, but experiments often show that this assumption is not valid and that the shape is non-axisymmetric deviating considerably from a rotational paraboloid [7–9] (Fig. 1). Other questions under discussion are the dynamics and the origin of dendritic sidebranching. What is the basic mechanism responsible for the initiation of sidebranches? Two mechanisms have been discussed, which might induce the formation of sidebranches: tip splitting, which includes oscillations in the growth rate, and the amplification of fluctuations at the sides of the dendrite.

In our studies we focus our considerations on the growth of three-dimensional xenon dendrites growing into a volume of pure supercooled melt. The exact shape of the dendrite tip and the origin of sidebranching are investigated. We have chosen xenon as a model substance for several reasons. Rare gases are simple substances amenable to detailed experimental studies. Rare gases form simple liquids, i.e., liquids that are composed of spherical atoms or molecules that are chemically inert. The most typical examples of substances forming simple liquids apart from rare gases are alkali metals [10]. Therefore, rare gases can be used as transparent model substances for metals. Rare gases have a low melting entropy. Therefore, they do not form facets and they are compatible with most theoretical models of dendritic solidification that assume a rough surface [2]. In Sec. II, a review of dendritic growth theories is presented with special emphasis on the results of theoretical models, which will be verified in our experiments. The setup of our experiment is described in Sec. III. In Sec. IV, the results of our measurements on xenon dendrites are presented and compared with current theo-

ries on dendritic growth. Finally, in Sec. V, these results are discussed. In our studies we have focused our considerations on the tip region, i.e., the region without sidebranches close to the tip. We determined the shape of the tip region of xenon dendrites with high spatial resolution and found that the shape deviates considerably from a parabola. In Sec. IV, experimental evidence is given that xenon dendrites grow in a stable mode and that thermal noise is the origin of sidebranching. To answer the question about the origin of sidebranching, we have performed measurements of the tip radius R and the tip velocity v_{tip} to find out whether xenon dendrites grow in a stable mode or tip oscillations can be observed. Theoretical models that assume that amplification of thermal noise is the origin of sidebranching make predictions of the amplification rate, i.e. growth rate, of the initial fluctuations that form the sidebranches later. In the experiment the amplification rate is not accessible directly, but can be measured indirectly by measuring the distance between the tip and the first sidebranch \bar{z}_{SB} , where the first sidebranch reaches a length of $1R$; see Sec. IIE. Furthermore, we show that the fractal dimension is a useful parameter to characterize the dendrite, especially in the region far away from the dendrite tip, where nonlinear interactions between sidebranches are important and coarsening takes place.

II. DENDRITIC SOLIDIFICATION

Most theoretical studies of dendritic growth assume a stationary growth in a pure supercooled melt of infinite extension [2,11]. For a pure substance the fundamental mechanism controlling the solidification process is thermal diffusion. The latent heat that is released during solidification heats the material in the neighborhood of the solidification front and must be removed before further solidification can take place.

The dimensionless thermal diffusion field around the dendrite is usually chosen to be

$$u = \frac{T - T_{\infty}}{L/c_l}, \quad (1)$$

where T is the local temperature and T_{∞} is the temperature far away from the dendrite. The ratio of the latent heat L to the specific heat of the liquid c_l is used as the unit of supercooling. The field u satisfies the diffusion equation

$$\frac{\partial u}{\partial t} = D_{\text{th}} \nabla^2 u, \quad (2)$$

where $D_{\text{th}} = \lambda_l/c_l$ is the thermal diffusivity, with λ_l being the thermal conductivity.

In the case of a solution, growth is limited by the diffusion of the solute and not by thermal diffusion. Thermal diffusion can be ignored as it is much faster than the diffusion of the solute. As a result, the concentration of the solute defines a diffusion field that plays almost exactly the same role as the thermal diffusion field u , with D_{th} replaced by the diffusion constant of the solute. This leads to a mathematical description of the problem that is almost identical to the case of the growth from a pure supercooled melt. Therefore we

restrict ourselves to the presentation of the theory of dendritic solidification from the pure supercooled melt.

Far away from the dendrite the diffusion field is $u_\infty=0$ according to Eq. (1). At the solidification front, boundary conditions are given by heat conservation and the local equilibrium temperature at the interface. The heat conservation can be written as

$$Lv_n = \lambda_s \hat{n} \nabla T_s - \lambda_l \hat{n} \nabla T_l, \quad (3)$$

where v_n is the normal growth velocity, \hat{n} is the unit vector normal to the interface, and λ_l and λ_s are the thermal conductivities of the liquid and the solid, respectively. The condition of the local equilibrium temperature at the interface [2] can be written as

$$u = \Delta - d_0 \kappa - \beta(v_n), \quad (4)$$

where the first term Δ is the dimensionless supercooling

$$\Delta = \frac{\Delta T}{L/c_l} = \frac{T_m - T_\infty}{L/c_l}. \quad (5)$$

T_m is the equilibrium melting temperature of the plane interface. The second term on the right-hand side of Eq. (4) is the Gibbs-Thomson correction for the melting temperature at a curved surface. κ is the curvature of the interface and

$$d_0 = \gamma_{sl} c_l T_m / L^2 \quad (6)$$

is the capillary length, which is proportional to the surface free energy of the solid-liquid interface γ_{sl} . The third term on the right-hand side of Eq. (4) is a kinetic correction. β describes a departure from local equilibrium at the moving interface and v_n is the velocity of the moving interface normal to the interface. Kinetic effects and anisotropies of surface properties influence β and γ_{sl} and play an important role in some recent dendritic growth theories; see Sec. II C. The diffusion equation and the moving boundary conditions lead to a rather complicated, nonlinear and nonlocal integro-differential equation that cannot be solved directly without further approximations. Usually, kinetic effects and sometimes even anisotropies of surface properties were neglected to simplify the problem. In the symmetric model [2], the thermal properties of the liquid and the solid are assumed to be the same. This assumption greatly simplifies some of the mathematics without losing too many important physical features. In the symmetric model the equation of motion can be written in closed form as

$$\begin{aligned} \Delta - \frac{d_0}{R} \kappa\{\xi(r, t)\} \\ = p^{3/2} \int_0^\infty \frac{d\tau}{(2\pi\tau)^{3/2}} \\ \times \int d^2 r' \exp\left(-\frac{p}{2\tau} [|r-r'|^2 + (\xi - \xi' + \tau)^2]\right) \\ \times (1 + \dot{\xi}'), \end{aligned} \quad (7)$$

where $\xi(r, t)$ denotes the instantaneous position of the solidification front at time t as observed in the frame of reference

moving at the steady-state growth velocity and ξ' denotes $\xi(r', t - \tau)$. Moreover, p is the so-called Péclet number defined in Eq. (11) and the curvature $\kappa\{\xi\}$ is given by

$$\kappa\{\xi\} = -\nabla \cdot \left(\frac{\nabla \xi}{[1 + (\nabla \xi)^2]^{1/2}} \right). \quad (8)$$

Here ∇ denotes the two-dimensional gradient. The symmetric model is the starting point for many theoretical studies of dendritic growth [2].

A. The Ivantsov solution

The ansatz that the shape of a dendrite can be satisfactorily approximated by a rotational paraboloid was suggested originally by Papapetrou [12]. An initial analytical approach to the steady-state dendritic heat flow problem was presented by Ivantsov [13,14]. Ivantsov neglected the anisotropy, the Gibbs-Thomson effect, and kinetic effects and found that the diffusion field around the dendrite can be solved exactly in axisymmetric parabolic coordinates. Ivantsov's solution is a shape-preserving dendrite growing at a constant tip velocity v_{tip} .

In this approximation the interface of the dendrite has the form of a rotational paraboloid and is given by the isotherm

$$u = \Delta. \quad (9)$$

In Ivantsov's solution the supercooling Δ is related to the Péclet number p

$$\Delta(p) = p e^p \int_p^\infty \frac{e^{-y'}}{y'} dy', \quad (10)$$

with the Péclet number defined as

$$p = \frac{v_{\text{tip}} R}{2D_{\text{th}}}. \quad (11)$$

The physical meaning of the Ivantsov solution has been a puzzle for many years. On the one hand, it was found in early experiments that the tips of real dendrites, especially those formed of materials with relatively low crystalline anisotropies such as most metals and several organic materials, looked more or less like rotational paraboloids. Moreover, several experiments seemed to indicate that Ivantsov's relation Eq. (10) was satisfied [4]. On the other hand, Ivantsov's solution is incomplete insofar as it provides only information on the product $v_{\text{tip}} R$, as can be seen in Eq. (11). This means that a continuous family of solutions of R and v_{tip} is found, whereas, in reality, experiments show a unique growth velocity v_{tip} and a unique tip radius R at a given supercooling. Furthermore, it turned out that Ivantsov's solution is manifestly unstable against sidebranching [15].

B. Stability constant σ^*

Considerable theoretical efforts have been directed to answering the question whether a second equation or length scale exists, which, combined with the Ivantsov solution, might select the unique dynamic operating state encountered in experiments. The introduction of surface tension as an

additional term in Eq. (9) led to a maximum in the $v_{\text{tip}}(R)$ curve. It was suggested that this maximum velocity may correspond to the dynamical operating state selected by the system. But this maximum-velocity hypothesis was disproved by the experiments with succinonitrile of Glicksman, Schaefer, and Ayers [16].

A more successful attempt to find a description of the operating state is due to Langer and Müller-Krumbhaar with the marginal-stability hypothesis [15]. Langer and Müller-Krumbhaar analyzed the stability of parabolic dendrites, treating surface tension as a linearized perturbation, and found that the continuum of Ivantsov's solutions is divided into a stable and an unstable region. It is assumed that the dynamical operating state selected by the physical system corresponds to the point of marginal stability dividing the stable and unstable regions. This hypothesis led to an additional relation between v_{tip} and R :

$$\sigma^* = \frac{2D_{\text{th}}d_0}{v_{\text{tip}}R^2}. \quad (12)$$

σ^* is usually referred to as the stability, selection, or scaling constant. For cubic crystals it was found that the value of the stability constant σ^* can be estimated to $\sigma^* \sim 0.026$, which is of the same order of magnitude as found in experiments [11]. In theories it is usually assumed that σ^* is independent of supercooling, but as $v_{\text{tip}}R^2$ is proportional to the volume solidification rate, which should vanish for $\Delta \rightarrow 0$, σ^* should show a dependence on supercooling at least in the limit $\Delta \rightarrow 0$.

Experimentally, it is found that the value of σ^* varies from substance to substance and seems to depend on supercooling for some substances [3,5,8,17]. It has been found [7–9] that R is not a well-defined quantity. Therefore the discussion whether or not $v_{\text{tip}}R^2 = \text{const}$ should be discussed again considering a careful redefinition of the quantity R .

C. Solvability theory

Further development in the theory of dendritic pattern selection was started with the so-called microscopic solvability theory [6]. The main insight of this theory is that the surface tension acts as a singular perturbation that imposes a solvability condition on the perturbed steady-state solutions. In contrast to the Ivantsov solution, only a discrete set of solutions exists and only one of these solutions is dynamically stable [6,18]. It is found that there are no stable solutions in the case of isotropic surface tension and that the anisotropy of the surface free energy is a prerequisite for the existence of a solution. It is interesting to note that the same stability constant σ^* found in the theory using the marginal stability hypothesis Eq. (12) is the relevant stability parameter again. This happens because one is looking for a small surface-tension-induced correction to the shape of the Ivantsov parabola, and in limit of small Péclet numbers, one encounters an equation quite similar to the one that arises in the marginal stability hypothesis [11].

It has been stated [19] that microscopic solvability theory has definitely resolved the dendritic pattern-selection problem. However, there are several reasons calling for caution. First, the underlying set of continuum equations is only an

approximation. The effects of microscopic crystal structure and growth kinetics are ignored and the effects of noise and sidebranching are also not included, which may play an important role at very small supercooling. Second, the present experiments do not confirm the predicted dependence of $\sigma^*(\alpha) \propto \alpha^{7/4}$ on the anisotropy strength α [20]. This may be due to the difficulty to obtain experimental values of the anisotropy sufficiently precise to permit definitive tests of the theory. Up to the present the microscopic solvability theory cannot be considered to be confirmed in all parts by experiments.

D. Nonaxisymmetric dendrites

The solvability theory in two dimensions has proven that an anisotropy of the surface tension is necessary to obtain stable growth [6]. Commonly, the anisotropy of surface tension is introduced by allowing the capillary length to depend on the orientation θ . In the case of a fourfold anisotropy, the capillary length is given by

$$d_0(\theta) = \bar{d}_0[1 - \alpha \cos(4\theta)], \quad (13)$$

where α is the anisotropy strength and \bar{d}_0 is the averaged capillary length. A straightforward extrapolation of the two-dimensional theory to the three-dimensional case is not possible because the anisotropy of surface tension gives rise to a nonaxisymmetric shape of the dendrite. This fact complicates the theory of three-dimensional nonaxisymmetric dendrites considerably. A numerical approach to the three-dimensional nonaxisymmetric dendrite problem was presented by Kessler and Levine [21]. Whereas in the two-dimensional case the solvability condition is associated with the smoothness of the tip, in the three-dimensional nonaxisymmetric case a solvability condition must be satisfied for each of the azimuthal harmonics [22]. Kessler and Levine made several approximations and performed a two-mode calculation. The crucial point is that enough degrees of freedom are found to satisfy all solvability conditions.

The first analytic theory of three-dimensional, nonaxisymmetric dendritic growth has been developed by Ben Amar and Brener [22]. The solvability condition for this problem provides a selection of both the growth velocity and the interface shape. The selected shape for a dendrite with a cubic anisotropy can be written in cylindrical polar coordinates (z, r, ϕ) as

$$z(r, \phi) = -\frac{r^2}{2} + \sum_m A_m r^m \cos(m\phi), \quad (14)$$

where all lengths are in units of the tip radius R . An important aspect of Eq. (14) is that the correction terms $r^m \cos(m\phi)$ grow faster than the underlying Ivantsov solution. Therefore this approximation is valid near the tip only and further away from the tip strong deviations from the Ivantsov parabola appear for any nonvanishing anisotropy. This is in contrast to the two-dimensional case, where for small anisotropies the selected shape is close to the Ivantsov parabola everywhere. In the theory of Ben Amar and Brener the first nonzero term of the shape correction found in the limit of small anisotropy ($\alpha \ll 1$) is

$$\xi_0 = -r^2 + \frac{1}{11}r^4 \cos(4\phi). \quad (15)$$

This formula represents a corrected (zeroth plus first order) shape for dendrites with cubic symmetry. It is independent of anisotropy strength. It will be shown in Sec. IV A that this form can be used to fit the contour of the dendrite tip very close to the tip (up to $2R$ away from the tip). The shape of the tip over distances of at least $18R$ from the tip can be described by a power law, as given in the following paragraph.

Recently, Brener has developed an analytical solution for the whole three-dimensional dendritic growth problem. The construction of the solution involves the existing three-dimensional selection theory of the dendrite [23] plus a matching of the tail region to this tip. In the case of a crystalline fourfold symmetry it is found that there are four fins growing at the sides of the dendrite. Close to the tip the shape can still be described by Eq. (14), but further away from the tip, where the shape begins to deviate strongly from the Ivantsov paraboloid, the shape is described in Cartesian coordinates (x, y, z) as

$$y(x, z) = (5|z|/3)^{2/5} \left(\frac{\sigma_2^*}{\sigma_1^*} \right)^{1/5} \left(\frac{x}{x_{\text{tip}}} \right)^{2/3} \int_{x/x_{\text{tip}}}^1 \frac{ds}{s^{2/3} \sqrt{1-s^4}}, \quad (16)$$

where the contour of the fins is given by the position of the top of the fins

$$x_{\text{ridge}}(z) = (5|z|/3)^{3/5} (\sigma_2^*/\sigma_1^*)^{1/5}, \quad (17)$$

where the function $\sigma_2^*(\alpha)$ is given by the two-dimensional selection theory. The ratio $\sigma_2^*(\alpha)/\sigma_1^*(\alpha)$ is independent of the anisotropy strength α in the limit of small α . Rewriting Eq. (17) leads to

$$z = a|x|^{5/3} \quad (18)$$

for the contour of the fins. The dimensionless prefactor a is expected to be of order unity [23]. In Sec. IV A, this result will be used in a comparison with our experimental data of the tip shape of xenon dendrites. It is found that the shape is almost independent of the material and growth parameters close to the tip Eq. (15) as well as in the region further away from the tip Eq. (18), where all lengths are measured in units of R .

E. Sidebranching

The occurrence of sidebranching in dendritic growth can in principle be attributed to the so-called Mullins-Sekerka instability [24]. Mullins and Sekerka showed that a planar solidification front growing in a supercooled or supersaturated melt is morphologically unstable. The interface is unstable against infinitesimal small perturbations if the wavelength of the perturbations λ is larger than the characteristic stability length λ_s of the system, which is given by

$$\lambda_s = 2\pi(d_0 l)^{1/2}, \quad (19)$$

where l is the macroscopic diffusion length, which is given by $l = 2D/v$ for a plane interface advancing with the growth velocity v . In this theory the basic principles have been developed to show how an initial, large enough perturbation grows and develops, as observed in sidebranching of dendrites. The origin of the initial perturbations that induce the formation of sidebranches has been a long-standing question. The theoretical aspects of this question are considered in this section and experimental results concerning the origin of sidebranching are presented in Sec. IV.

Two different scenarios that might induce the initial perturbations and the formation of sidebranches have been discussed in the literature. In the first scenario, tip splitting or dynamical tip oscillations have been proposed as the origin of sidebranching. In this case it is argued that nonlinear aspects of the equation of motion can lead to a stable oscillating growth mode [25], which can act as the source of the sidebranching. Tip splitting has been observed during growth from solutions in thin cuvettes [26] and is well known to occur in viscous fingering phenomena. Tip oscillations lead to a more or less periodic appearance of the sidebranches and to a correlation between sidebranches growing on opposite sides of the dendrite. However, in many experiments no such tip oscillations and no correlation between the sidebranches are observed.

In the second scenario, sidebranching is assumed to be driven by selective amplification of noise [27–29]. Numerical and analytical studies of the two-dimensional boundary model with both kinetic and surface tension anisotropy [27] show that a single perturbation of the tip moves away from the tip with v_{tip} . Therefore, continually generated perturbations are needed for a continuous train of sidebranches. Similar results have been obtained by numerical and analytical studies of two-dimensional nonlocal models.

We will show that our experiments allow us to rule out tip splitting in the case of xenon dendrites growing into a three-dimensional volume. Therefore, we focus our considerations on the amplification of noise.

Langer [28] studied the time-dependent behavior of sidebranching deformations for an axisymmetric dendrite in the three-dimensional symmetric model; see Eq. (7). The first step in this analysis is a linearization about the Ivantsov parabola

$$z = \xi(r, t) = -r^2/2 + \xi_0(r) + \xi_1(r, t), \quad (20)$$

where both $\xi_0(r)$ and $\xi_1(r, t)$ are small correction terms. The time-independent function $\xi_0(r)$ is a smooth shape correction due to nonzero surface tension and $\xi_1(r, t)$ is the time-dependent perturbation. As usual, lengths are measured in units of R and times in R/v_{tip} .

The analysis of the equation of motion in the WKB approximation lead to the following result: The perturbations generated near the tip grow in amplitude, stretch, and spread as they propagate down the dendrite in such a way that they remain stationary in the laboratory reference frame. In the linear approximation the amplitude of the perturbations grows exponentially with the distance z from the dendrite tip with an exponent proportional to $(|z|^{1/4}/\sigma_1^{*1/2})$. This behavior implies that noise in the solidifying medium is selectively amplified in such a way that a fluctuating train of side-

branches is produced, which is in qualitative agreement with experimental observations. Moreover, Langer studied the response to thermal fluctuations in order to test whether thermal fluctuations are strong enough to account for the experimentally observed sidebranching.

An advantage of the symmetric model, in contrast to other models, such as the boundary-layer model, is that the symmetric model is based on a realistic description of the thermal field and there is no difficulty in adding thermal fluctuations. The appropriate procedure for introducing thermal noise into a system like that is to add a fluctuating heat source $S(r, z, t)$ to the thermal diffusion equation. The autocorrelation function of the source term is chosen so that the known thermodynamic fluctuations of the diffusion field are reproduced. The fluctuation strength \bar{S} is given by [28]

$$\bar{S}^2 = \frac{2k_B T^2 c_l D_{th}}{L^2 v_{tip} R^4}. \quad (21)$$

k_B is the Boltzmann constant. Langer simply repeated the analysis of the time-dependent behavior of sidebranching deformations mentioned above, but now with \bar{S} added as an additional stochastic term to the equation of motion [Eq. (7)] and obtained

$$\langle \xi_1^2(r) \rangle^{1/2} \approx \bar{S} \bar{C} \sigma^{*1/8} r^{3/8} \exp\left[\frac{2}{3} \left(\frac{2r}{3\sigma^*}\right)^{1/2}\right] \quad (22)$$

for the root-mean-square amplitude $\langle \xi_1^2(r) \rangle^{1/2}$ of the sidebranches generated by thermal fluctuations. \bar{C} is a constant of order unity.

It is not possible to verify the growth rate of sidebranches as predicted by Eq. (22) in an experiment directly. Equation (22) is valid only close to the tip, and in this region the sidebranches are too small to measure the growth rate directly. One way to test the predictions of the growth rate of sidebranches is to ask how far down along the dendrite one must go in order to find a root-mean-square amplitude of the sidebranches to be equal to some arbitrarily chosen, visible fraction of R . For this purpose, we use the mean distance \bar{z}_{SB} between the tip and the position where sidebranches have a root-mean-square amplitude of $\langle \xi_1(z)^2 \rangle^{1/2}$ of about $1R$; see Fig. 2. \bar{z}_{SB} can be used as a measure for the growth rate of sidebranches. The larger the growth rate, the smaller \bar{z}_{SB} and vice versa. Following the theory of Langer [28], the position of the first sidebranch is given by

$$\bar{z}_{SB} \approx \frac{\sigma^{*2}}{2} \left(\frac{3}{2}\right)^6 \ln^4(\bar{S}\bar{C}) \quad (23)$$

for an axisymmetric dendrite in the framework of the symmetric model.

By comparing the predictions of Eq. (23) with the experimental results of Huang and Glicksman [4], Langer found that thermal noise seems to be too small by 1–2 orders of magnitude to explain the experimentally observed sidebranching. However, the slow decrease of \bar{z}_{SB} with increasing supercooling is supposed to be in qualitative agreement with experimental observations. Langer proposed tip oscillations as an alternative model to describe sidebranching.

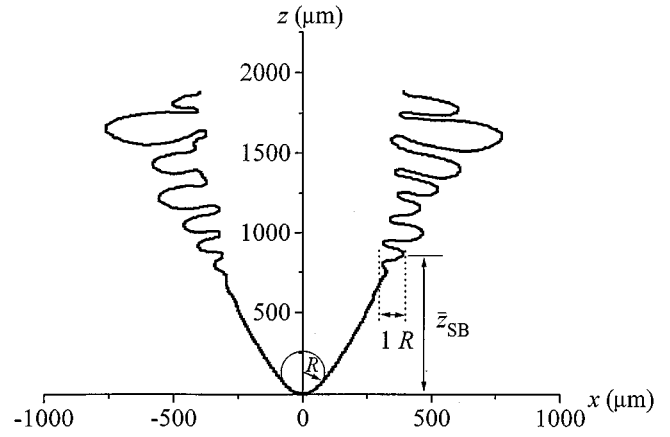


FIG. 2. Rotated and translated contour of a xenon dendrite. z is along the growth direction and x is the width of the dendrite. \bar{z}_{SB} is the mean distance between the tip and the position where the sidebranches have a root-mean-square amplitude of $1R$. R is the radius of curvature at the tip.

Brener and Temkin extended the analysis of the time-dependent behavior of sidebranching taking into account the actual nonaxisymmetric shape of a three-dimensional dendrite [29]. They used an analytic approach that has been developed in Ref. [30] and is slightly different from the above-mentioned approach of Langer [28]. According to Brener and Temkin, the root-mean-square amplitude $\langle \xi_1^2(z, y) \rangle^{1/2}$ for the sidebranches generated by thermal fluctuations can be written as

$$\langle \xi_1^2(z, y) \rangle^{1/2} \sim \bar{S} \exp\left\{ \frac{2(5/3)^{9/10}}{3\sqrt{3}\sigma^*} |z|^{2/5} \left[1 - \frac{9}{4} \left(\frac{3}{5}\right)^{4/5} \times (\sqrt{1-i/9} - 1) \frac{y^2}{|z|^{4/5}} \right] \right\}, \quad (24)$$

where $\xi = x, y, z$ are the spatial, Cartesian coordinates of the dendrite and \bar{S} is the same fluctuation strength as introduced in Eq. (21). The important point in Eq. (24) is that the amplitude grows exponentially as a function of $(|z|^{2/5}/\sigma^{*1/2})$, which is faster than in the axisymmetric case [28], where the amplitude grows exponentially as a function of $(|z|^{1/4}/\sigma^{*1/2})$. Brener and Temkin argue that the effect that the growth rate is faster in the nonaxisymmetric case might resolve the puzzle that experimentally observed sidebranches have much larger amplitudes than can be explained by thermal noise in the framework of the axisymmetric approach [28].

Again \bar{z}_{SB} can be used to test the predicted growth rate of sidebranches Eq. (24). In the framework of Brener and Temkin the position \bar{z}_{SB} of the first sidebranch is found to be

$$\bar{z}_{SB} \approx \frac{(27\sigma^*)^{5/4}}{2^{5/2}(\frac{5}{3})^{9/4}} |\ln \bar{C}\bar{S}|^{5/2}. \quad (25)$$

The position of the first sidebranch \bar{z}_{SB} can be measured directly in dendritic growth experiments and can be used to test the theoretical predictions of Refs. [28], [29] [Eqs. (23) and (25)].

F. Fractal structure

Far away from the dendrite tip, where the sidebranches are larger, nonlinear interactions between neighbored sidebranches are becoming important and coarsening takes place. It is found that, in the region far away from the tip, the parameters that characterize individual sidebranches, such as the length or the spacing of sidebranches, do not lead to reproducible results [7]. This behavior is typical for dynamical chaotic systems. It is found that “integral” parameters, which describe properties of the integral dendrite, are suitable to characterize dendrites as these “integral” parameters take account of the nonlinear interactions among the different sidebranches. Integral parameters are, e.g., the volume or the surface area or the contour length of a projection of a dendrite [7]. Another integral parameter is the fractal dimension d_f of the dendrite. For a review of fractals and fractal dimensions see Ref. [31]. There are two widely used methods to determine the fractal dimension of an experimental data set, e.g., the box counting method and the “correlation dimension” method. The “box counting” method can easily be derived from the definition of the fractal dimension

$$d_f = \lim_{\epsilon \rightarrow 0} \frac{\ln N(\epsilon)}{\ln(1/\epsilon)}, \quad (26)$$

where $N(\epsilon)$ is the minimum number of “boxes” (squares or circles in two dimensions) needed to cover the entire fractal set. ϵ corresponds to the size, e.g., length or diameter, of these boxes. In physical systems it is not possible to take the limit $\epsilon \rightarrow 0$, but for small ϵ the number of boxes $N(\epsilon)$ has an asymptotic behavior of the form

$$N(\epsilon) \sim \frac{1}{\epsilon^{d_f}}. \quad (27)$$

Taking the logarithm on both sides of Eq. (27) leads to the linear relationship

$$\ln N(\epsilon) \sim -d_f \ln \epsilon, \quad (28)$$

which can be used to calculate the fractal dimension d_f . The fractal dimension calculated in this way is commonly called box dimension. In practice, the linear relationship of Eq. (28) holds only over a limited range. The scaling behavior breaks down for values of ϵ smaller than the typical minimal distances of the system such as the pixel size and for values of ϵ larger than size of the entire system. In the case of the fractal dimension of xenon dendrites, the scaling range is limited, on the one hand, by the tip radius or the pixel size, depending on magnification, and, on the other hand, by the overall size of the dendrite.

When computing the box dimension, it is not always easy to find a minimal covering of the fractal set. There is an equivalent way to compute the box dimension that avoids this problem. Instead of looking for a minimal covering of the set with boxes of side ϵ , one covers the fractal set with a square mesh of side ϵ , i.e., regularly placed, nonoverlapping boxes of side ϵ , and determines the number $N(\epsilon)$ of these nonoverlapping boxes needed to cover the entire set. Afterward the fractal dimension is computed as before. Although the covering of the set is not minimal, this method

usually delivers good results. Even with this improvement, the box dimension has the drawback that its computation requires much storage space and computing time. Therefore, box counting is rarely used to calculate the fractal dimension of large fractal sets. For xenon dendrites, however, box counting can be used, as the fractal set, i.e., the contour of the dendrite, is small, consisting only of about 3000–4000 data points.

A second widely used method, which is known as the correlation dimension method, has been developed by Grassberger and Procaccia [32]. The approach relies on correlation functions and is more efficient than box counting. The correlation function $C(r)$ is defined as

$$C(r) = \lim_{m \rightarrow \infty} \frac{1}{m^2} \sum_{i,j=1}^m H(r - |\vec{x}_i - \vec{x}_j|), \quad (29)$$

where r is a radius of a hypersphere in the n -dimensional embedding space, m is the number of points in the fractal set, and \vec{x}_i, \vec{x}_j are coordinates of points in the set. H is the Heavyside function defined by $H(x) = 1$ for positive x and 0 otherwise. Roughly speaking, $C(r)$ measures the density of points within a “circle” with radius r as a function of r . Grassberger and Procaccia showed that

$$C(r) \sim r^\nu, \quad (30)$$

or taking the logarithm on both sides

$$\ln C(r) \sim \nu \ln r, \quad (31)$$

where ν is the correlation dimension. This linear relationship can be used to estimate the fractal dimension ν . It is found that in general $d_f > \nu$, although usually $d_f \approx \nu$ [32]. As in the case of box counting, the linear relationship Eq. (31) holds only over a limited range and again the range is limited by the tip radius and the overall dimensions of the dendrite.

Numerical calculations of fractal dimensions are often difficult and sometimes may lead to inconclusive results, e.g., if too few data points are available [33]. To obtain a physically meaningful and reproducible fractal dimension the scaling range should be more than one order of magnitude. Furthermore, one may use more than one method to calculate the fractal dimension in order to check the results.

Brener, Müller-Krumbhaar, and Temkin proposed a phase diagram for the selection of growth patterns in diffusional growth [34]. This classification scheme gives the dependence of the growth habit on supercooling and anisotropy. It discriminates between fractal structures with fractal dimension $d_f < d$, with d being the dimension of the space where the experiment takes place, and nonfractal structures, which are called compact. It is argued that a “true” fractal can occur in the limit of $\Delta = 0$ only, where the correlation length becomes infinite. In analogy to equilibrium phase transitions this can be understood as a critical point. For $\Delta \neq 0$ self-similar fractal properties may still exist over an intermediate range of length scales. Furthermore, a distinction was made between dendritic structures with a pronounced orientational order and structures without an apparent orientational order, which are called seaweed. It is found that at small anisotropies the structure is dendritic, whereas the structure becomes compact

at larger anisotropies. The structure is fractal at small supercoolings and seaweedlike at larger supercoolings. Therefore, at small supercoolings and small anisotropies a fractal dendritic structure of the growing crystal is expected. For very large supercoolings the phase diagram breaks down, as in this region growth is controlled by attachment kinetics.

If one assumes that thermal diffusion or solute diffusion are the only rate controlling processes in dendritic solidification, which is the case for xenon dendrites, then it seems to be a consequent development to study the dendritic solidification in the framework of diffusion-limited aggregation (DLA) [31]. DLA structures arise naturally when studying phenomena such as electrochemical deposition, viscous fingering, chemical dissolution, and the rapid crystallization of lava [35]. The rule defining DLA is simple, like many models in statistical mechanics. Random walkers are released from a large circle surrounding the growing cluster placed at the origin. When a random walker touches a site at the interface of the cluster, it sticks and the cluster has grown by one particle. In two dimensions this type of aggregation process produces clusters that have a fractal dimension of $d_f=1.71$. DLA is very sensitive to noise and anisotropies of the underlying discrete lattice. Various techniques for noise reduction and suppression of lattice anisotropies have been invented [35]. Nittmann and Stanley have studied dendritic solidification in the framework of DLA and simulated the growth of two-dimensional dendrites and found patterns that resemble two-dimensional projections of real dendrites [36]. A fractal dimension of $d_f=1.5$ was found in the simulations.

Arneodo *et al.* studied the statistical properties of two-dimensional anisotropic diffusion-limited aggregates grown in a strip [37]. They found an anisotropy induced crossover from isotropic DLA clusters with a fractal dimension of $d_f=5/3$ to dendritic fractal patterns with a fractal dimension of $d_f=3/2$.

G. Simulations

During the past years, many computer simulations have been performed. The nonlinear nature of the equations of motion in dendritic growth makes analytic studies difficult and often numerical simulations have proven to be the only way for further progress. Several models have been used for simulations: the geometric model [38], the boundary layer model [27,39], or fully nonlinear models [40]. Numerical simulations were carried out for the fully nonlinear model and the dependence of the growth velocity on anisotropy was investigated [41]. Most of these simulations are limited to two dimensions. This is due to the enormous computing power needed for these simulations. Even two-dimensional simulations require often the fastest supercomputers, making three-dimensional simulations virtually impossible. However, diffusion in two dimensions is qualitatively different from diffusion in three dimensions. Because of this it is not easy, or almost impossible, to compare results of two-dimensional simulations to experimental results of three-dimensional dendrites.

Kobayashi nevertheless succeeded in simulating three-dimensional dendritic growth [42]. The simulations were performed for various noise and anisotropy strengths. For certain values of the noise and anisotropy strength the pic-

tures of the simulated dendrites look much like three-dimensional xenon dendrites. Kobayashi included a sort of cubic anisotropy and found, as in the case of xenon dendrites, that four fins grow along the dendrite stem and that the sidebranches develop at the ridges of these fins. Kobayashi used the so-called phase field model. The big advantage of the phase field model, compared to other models, is that the interface is represented only implicitly. Therefore, the equations of motion become much simpler, as there are no more moving boundary conditions. This fact makes it possible to simulate dendritic growth qualitatively in three dimensions. The phase field $p(r,t)$, which is an order parameter, represents the phase of the solidifying material. $p(r,t)=0$ means liquid and $p(r,t)=1$ means solid, where r is the position and t the time. The interface of the crystal is represented in $p(r,t)$ by the transition layer connecting the liquid and the solid phase and can be determined by differentiating the phase field $p(r,t)$.

The main problem about the phase field model is the finite thickness ϵ of the interface. For quantitative simulations it is required that ϵ is much smaller than the typical lengths of the system, i.e., $\epsilon \ll R$ in dendritic solidification. Quantitative simulations are not possible at present as small values of ϵ demand for a small grid mesh size increasing the computing time and size of memory needed for the simulations, which are beyond the capabilities of computers available today.

III. EXPERIMENTAL SETUP

The experimental setup is similar to the one used in previous experiments with xenon dendrites [7]. For our experiments we have chosen xenon as a model substance. The choice of pure xenon has several advantages in comparison to (i) solute systems and (ii) the growth of dendrites from organic materials.

(i) For a pure system the tip radius R is typically of the order of 50 μm [3,4], whereas in solute systems R is typically 2 μm [8,43]. The optical resolution is limited by diffraction. The maximum optical resolution that can be achieved in experimental systems is of the order of the wavelength of light, which is about 0.5 μm in the visible spectrum. Thus pure systems can provide data on the shape of the tip with much higher accuracy than solute systems with comparable growth velocities. In addition to that, in solute systems both concentrations and temperature have to be controlled, whereas in pure systems temperature has to be controlled only and the homogenization of temperature is much faster than solute homogenization because of the high thermal diffusivity.

(ii) Xenon can be purified easily because rare-gas purifiers are available, which are used in semiconductor processing. Finally, xenon does not decompose at the melting temperature in contrast to many organic materials.

Selected properties of xenon are summarized in Table I. As far as we know, experimentally determined values of the solid-liquid interfacial free energy γ_{sl} of xenon do not exist. Only a rough estimate can be made if one assumes that γ_{sl} is proportional to the heat of fusion L per surface atom [44]. However, the capillary length d_0 , which is an important length scale in dendritic growth theories, is proportional to γ_{sl} [Eq. (6)]. Therefore, experimental measurements of γ_{sl}

TABLE I. Selected properties of xenon.

Molecular weight	M_m	131.30	g/mol
Triple-point temperature	T_t	161.3897	K ^a
Triple-point pressure	p_t	0.816901	bar ^b
Triple-point molar volume (l) ^j	$V_m(l)$	44.31	cm ³ /mol ^c
Triple-point molar volume (s) ^j	$V_m(s)$	38.59	cm ³ /mol ^c
Heat of fusion	L	2299	J/mol ^d
Melting entropy	ΔS_m	14.24	J/mol K
Jackson α -factor	α_{Jackson}	1.71	i
Specific heat (l)	$c_p(l)$	44.6	J/mol K ^d
Specific heat (s)	$c_p(s)$	36.0	J/mol K ^d
Thermal conductivity (l)	λ_l	0.734×10^{-3}	W/cm K ^e
Thermal conductivity (s)	λ_s	4.76×10^{-3}	W/cm K ^e
Thermal diffusivity (l)	$D_{\text{th}}(l)$	7.29×10^{-4}	cm ² /s
Thermal diffusivity (s)	$D_{\text{th}}(s)$	4.96×10^{-3}	cm ² /s
Refractive index (l)	n_l	1.3957	f
Refractive index (s)	n_s	1.4560	g
Solid-liquid interfacial free energy	γ_{sl}	1.073×10^{-8}	J/cm ^{2h}
Capillary length	d_0	4.9×10^{-8}	cm
Unit of supercooling	Θ	59.2	K

^aReference [45].^bReference [52].^cReference [53].^dReference [54].^eReference [55].^fReference [56].^gReference [57].^hEstimate according to Ref. [44].ⁱMaterials with $\alpha < 2$ are usually not faceting in contact with the melt.^j l liquid; s , solid

and its anisotropy would be important for a further verification of dendritic growth theories. For dendritic growth experiments it is essential to have a thermally well controlled surrounding of the xenon. For this purpose we use a cryostat as depicted in Fig. 3. Liquid nitrogen can be used for cooling because xenon has a relatively high melting point compared to the other rare gases.

The cryostat consists of a double-walled glass vessel, which is surrounded by liquid nitrogen. The glass vessel is filled with isopentane as thermostating liquid. We use isopentane as the thermostating liquid because of its large liquid range (-159.9°C to $+27.9^\circ\text{C}$, at atmospheric pressure). The space between the walls of the vessel is filled with helium gas. The gas pressure is used to control the thermal contact between the isopentane and the liquid nitrogen. The helium pressure is chosen in such a way that the isopentane is cooled slightly too much. This cooling is compensated by counterheating with about 10 W. The temperature stability of the xenon that can be achieved this way is better than $\pm 10^{-4}$ K during several hours. This temperature stability is necessary. For example, v_{tip} can be measured with a precision of about $\pm 2\%$. As $v_{\text{tip}} \sim \Delta T^{1.745}$ and typical supercoolings are in the range $20 \text{ mK} \leq \Delta T \leq 150 \text{ mK}$, the control parameter, i.e., the supercooling, has been known to about $\pm 1\%$.

The growth vessel is immersed completely in the isopentane and a laminar flow is induced in the isopentane by a stirrer, providing a homogeneous temperature distribution around the growth vessel. The volume of the growth vessel is about 100 cm^3 . This volume is large enough to be considered ‘infinite.’ This has been verified in earlier studies [3,5].

Trivedi and Mason [5] have shown that the effect of container walls will be negligible for $\Delta T > 8.5 \times 10^{-6}$ K. During the experiment the growth vessel is filled with pure, liquid xenon. The temperature of the melt is measured by two fused-in platinum resistors in the growth vessel and ac measuring techniques.

The experiments are performed at conditions close to the triple point ($T_t = 161.3897$ K). Triple points of rare gases are well defined, they are used as calibration points in thermometry [45]. Special attention is paid to the purity of the xenon. The xenon gas with a purity of 99.998% was supplied by Linde. $C_m H_n$, CO_2 , O_2 , N_2 , H_2 , and H_2O are extracted by a rare-gas purifier to 99.9999% prior to every run [46]. Therefore no disturbance of the dendritic growth by impurities has to be expected.

At the beginning of the experiment the liquid xenon is cooled to T_∞ several mK below the melting point and crystal growth is initiated by the capillary injection technique. A capillary is inserted from above into the growth vessel (Fig. 4). At the upper end of this capillary, a seed is nucleated by cooling with a Peltier element. This seed grows down inside the capillary. The seed exits the capillary in the middle of the growth vessel and starts to grow freely, dendritically into the supercooled melt with the initially homogenous temperature T_∞ . The main stem of the dendrite grows along the [001] direction.

The capillary is rotatable. This allows us to orient the dendrites in such a way that two of the fins are in the object plane, i.e., the crystallographic [001] axis is oriented along the optical axis of the optical system. A rotatable capillary is

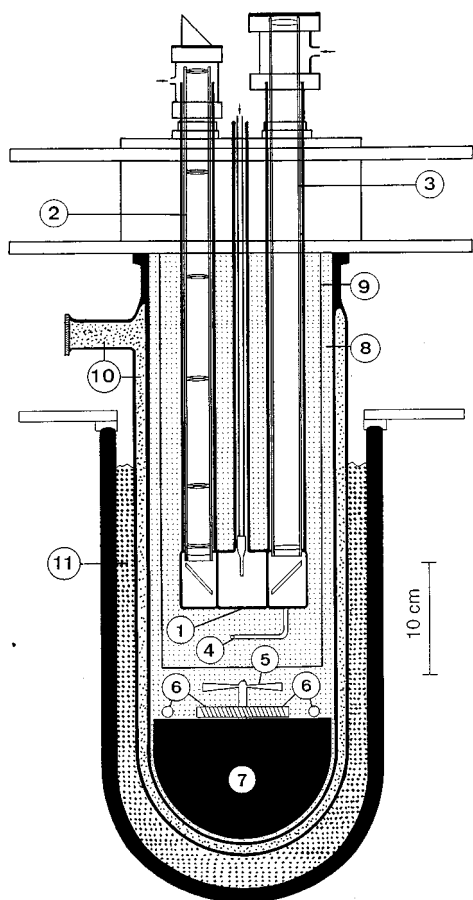


FIG. 3. Cryostat. 1, growth vessel; 2, periscope; 3, illumination system; 4, temperature sensor in the thermostating liquid; 5, stirrer driven from outside the cryostat; 6, heater; 7, a big mass of stainless steel to reduce the vibrations of the stirrer (the growth vessel is fixed independently of the stirrer system); 8, thermostating liquid: isopentane; 9, tube to provide a laminar flow of the thermostating liquid; 10, adjustable vacuum to control cooling power; 11, liquid nitrogen.

crucial for the determination of the nonaxisymmetric shape of the dendrite tip.

The optical system consists of an illumination system and a self-built periscope for the observation of the growing dendrite. The periscope consists of a system of achromatic lens pairs. The optical resolution of the periscope is $1 \mu\text{m}$, which is close to the theoretical limit. The resolution was tested by means of a graticule.

The periscope and the illumination system are placed separately in glass tubes (under helium gas atmosphere) on opposite sides of the cylindrical growth vessel (Figs. 3 and 4). Both the periscope and the illumination system are at the same temperature as the liquid xenon in the growth vessel, separated from the liquid xenon by optical windows only. Therefore undisturbed images with high resolution of the growing dendrite are obtained.

The difference between the refractive indices of liquid and solid xenon is only $\Delta n_{sl} = 0.0589$. Because of this small difference, a special illumination system is needed to obtain pictures with high contrast. We use an illuminated, diffusive scattering glass plate that is imaged in a plane behind the

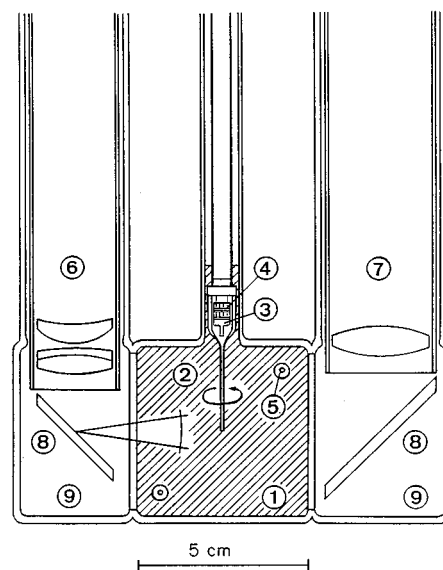


FIG. 4. Growth vessel. 1, liquid xenon; 2, rotatable capillary; 3, upper end of capillary where nucleation occurs; 4, Peltier element for cooling; 5, fused-in platinum resistor (temperature sensor); 6, periscope; 7, illumination system; 8, mirror; 9, helium atmosphere.

growing dendrite. Monochromatic light improves the contrast. Light with a wavelength of 546 nm , for which the achromats of the periscope were designed, was chosen for illumination. This illumination leads to highly contrasted pictures with a dark dendrite and a bright background (Fig. 1).

The dendrites are imaged on the chip of a charge coupled device (CCD) camera, which is interfaced to a commercial SVHS video recorder with a time code generator. The pictures from the video tape are digitized with a frame grabber (Matrox). The frame grabber is working with a resolution of 512×512 pixels, 8-bit gray scale. High optical magnification has been chosen to provide the resolution of $1 \mu\text{m}$ per pixel at the digitized pictures. The resulting magnification of the digitized pictures is calibrated with the outer, known diameter of 0.385 mm of the inserted capillary. However, for the measurements of the fractal dimension a lower magnification had to be used to allow the whole dendrite to be imaged on a picture. Because of the limited number of pixels of the CCD camera the resolution of the digitized images was limited to about $10 \mu\text{m}$ per pixel in this case.

In the next step the contour of the dendrites is extracted from the digitized video pictures. In previous measurements with xenon dendrites [7] edge detection was performed by first thresholding the image and then following the contour in the resulting binary image. This procedure has the disadvantage that an arbitrary value for the threshold has to be chosen manually. Furthermore, this procedure extracts the contour correctly for highly contrasted images only. In our analysis of tip oscillations, where time sequences of several hundred pictures had to be extracted, it was not feasible to choose a threshold for every picture manually. Therefore a new, fully automatic algorithm for contour extraction was developed.

The algorithm works by convolving the image with a Laplacian of a Gaussian. This transformation applies the Laplacian operator and filters the image with a Gaussian at the

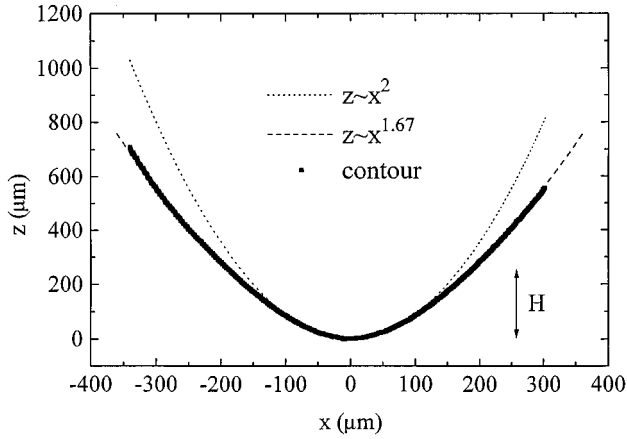


FIG. 5. Data of the contour of a dendrite in the tip region are compared with a power-law fit with $\beta=1.67$. The size of the squares is much larger than the error of the measurements. The plotted parabola demonstrates that the shape deviates considerably from the parabola. H indicates the fitting height.

same time [47]. The filtering of the image with a Gaussian is necessary as the Laplacian operator is very sensitive to noise in the intensity of the image. Now the edge points can be marked as the zero crossings of the Laplacian, i.e., the points where the Laplacian switches from positive to negative values and vice versa. This algorithm guarantees that closed and only one-pixel-wide contours of the dendrites are detected in a robust way. The drawback of this algorithm is that convolving the image with a Laplacian of a Gaussian is computationally very demanding, but with a fast workstation this problem can be solved. The edge detection was performed on a *silicon graphics* workstation. Taking about 10 min per image, the whole time sequence of images could be extracted in a batch mode overnight. Afterward, the extracted contour data have been analyzed with mathematical standard software packages such as MAPLE and MATHEMATICA.

IV. EXPERIMENTAL RESULTS

A. Tip shape

Xenon crystallizes in a fcc structure leading to a nonaxisymmetric dendrite with fourfold symmetry. Even the tip region is not axisymmetric. Four fins grow along the dendrite, starting immediately behind the tip. The sidebranches grow at the ridges of these fins (Fig. 1).

In agreement with earlier studies with pure melt [7] and experiments with crystallization from a solution [8], we find that the contour of the dendrite, even in the tip region, does not have a parabolic shape (Fig. 5). In all our experiments we orient the dendrites in such a way that two of the fins are in the object plane, i.e., the crystallographic [001] axis is oriented along the optical axis of the periscope. There is a fundamental difficulty in quantifying the dendrite tip shapes. In order to obtain the radius of curvature at the tip, it is necessary to use data points obtained from regions of the contour away from the very tip. Fitting the contour of the dendrite tip by a simple parabola for the calculation of the tip radius leads to a dependence of the tip radius on the fitting height H . H is the distance from the tip, along the z axis, up to which data points of the contour are included for fitting. It is

found that the larger the H the smaller the fitted curvature, i.e., R increases with increasing H . In order to obtain a well-defined reproducible value for the tip radius, one has to define some kind of averaging. Considering only a small portion very close to the tip, one uses only very little data points of the contour, therefore one obtains large statistical errors. Averaging over a larger range of the dendrite tip means the inclusion of many data points that do not approximate well the parabola fit at the very tip. Dougherty and Gollub [8] have fitted over an arbitrary length of the dendrite of $H=3R$. This is a possible compromise. Using a parabola for fitting, Hürlimann *et al.* [7] have determined the tip radius R as a function of the fitting height H for various values of H . A linear dependence of the tip radius on H was found. Hürlimann *et al.* extrapolated the tip radius for $H \rightarrow 0$, obtaining a well-defined limiting tip radius R_{tip} in this way,

$$\lim_{H \rightarrow 0} R(H) = R_{\text{tip}}. \quad (32)$$

In experiments with xenon dendrites [7] the dependence of R_{tip} on supercooling is found to be

$$R_{\text{tip}} = (5.2 \pm 0.4) \times \Delta T^{-0.83 \pm 0.03}, \quad (33)$$

where R_{tip} is measured in micrometers and ΔT in degrees kelvin. It is interesting to note that $v_{\text{tip}} R_{\text{tip}}^2 = \text{const}$ in the case of the limiting tip radius R_{tip} .

For a better approximation of the tip shape, we have tried to fit several low-order polynomials of the form

$$z = \sum_{i=0}^n a_i x^i, \quad (34)$$

with n in the range 3–7. z is measured along the growth direction and x is the width of the dendrite; see Fig. 2. Fits with polynomials of order higher than $n=7$ have proven to be numerically unstable. We have found that a low-order polynomial can approximate the shape of the dendrite in the tip region much better than a simple parabola fit [48,49]. However, the tip radius R calculated by means of polynomial fits still shows a dependence on the fitting height H used for fitting. The dependence on the fitting height H is much smaller than in the case of a parabola fit, but nevertheless it cannot be neglected. The tip radius R of the polynomial fits was calculated using the formula of the radius of curvature in two dimensions, which is given by

$$R = \frac{1}{\kappa} = \frac{[1 + f'(x)^2]^{3/2}}{f''(x)}. \quad (35)$$

Furthermore, the calculated tip radius R shows a dependence on the order of the polynomial used for fitting and no order of the polynomials can be found that fits the contour best, i.e., has the smallest standard deviation or the smallest, or no, dependence of R on the fitting height H . This makes it even more difficult to determine a tip radius in a well-defined reproducible way. Based on these experimental results we conclude that the shape of the contour in the tip region cannot be described accurately by a parabola or a low-order polynomial.

As an alternative we tried to fit the contour by a power law of the form

$$z = a|x|^\beta. \quad (36)$$

A power-law fit can be seen as a generalization of the simple parabola fit, coinciding for $\beta=2$ with the parabola fit. The main advantage of the power law fit is that there are only two fitting parameters a and β , whereas polynomial fits of order n have $n+1$ fitting parameters. Polynomial fits introduce many additional fitting parameters and the physical meanings of these parameters are not obvious. For the power-law fit the physical meanings of the two parameters α and β are known and theoretical predictions exist [23].

Using images with high resolution ($1 \mu\text{m}$ per pixel), we performed this power-law fit for several dendrites grown at various supercoolings in the range $20 \text{ mK} \leq \Delta T \leq 150 \text{ mK}$ and found that the contour in the tip region can be approximated much better with the power-law fit than with a parabola or a low-order polynomial fit. An exponent of $\beta = 1.67 \pm 0.05$ is found for all dendrites independent of supercooling [50]. Figure 5 shows the contour of a xenon dendrite in the tip region as found in our experiments. The power-law fit with $\beta = 1.67$ is plotted in this figure. The parabola plotted in Fig. 5 demonstrates that the shape of the contour deviates considerably from a parabola for $H > 2R$. The standard deviation of the power-law fit is only $1.5 \mu\text{m}$, which is close to the resolution of the image data ($\sim 1 \mu\text{m}$). In contrast to the parabola or polynomial fits the power-law fit does not depend on the fitting height H . This can be seen from the fact that the power-law fit approximates the contour beyond the range used for fitting. In Fig. 5 contour points up to a fitting height of $250 \mu\text{m}$ are used for the fit. A power-law fit matches the contour beyond that region at least to $H = 18R$ within the precision of the measurements. The fit starts to deviate from the contour in the region where the first sidebranches appear. The value of $\beta = 1.67$ of the fitted contour of the fins is in good agreement with the analytical studies of Brener and Temkin presented in Sec. IID. Brener and Temkin predict that the contour of the fins of nonaxisymmetric dendrites with cubic symmetry can be described by a power law Eq. (18) with $\beta = 5/3$.

Moreover, we use our data to test the prediction that even for nonaxisymmetric dendrites very close to the tip ($H < 2R$) a parabolic, axisymmetric tip shape is still preserved [21,22]. Very close to the tip the contour extraction is less precise $\pm 4 \mu\text{m}$ because of the reduced sharpness of the images in this region that is due to the larger thermal gradients around the tip that disturb the imaging process. Figure 6 shows the data of the contour of a xenon dendrite in the region very close to the tip ($H < 2R$). A power-law fit with $\beta = 1.67$ and a parabola fit are plotted together with a fit as proposed by Ben Amar and Brener, which is a parabolic fit with an additional correction term due to anisotropy Eq. (15).

All three fits match the contour data within experimental errors. Therefore, very close to the tip the shape of the contour can be approximated by a parabola and a radius of curvature R_{tip} can be determined in this limited region in a reproducible way. However, statistical errors become significant, as only a small number of data points can be used in the determination of R_{tip} . Our data are compatible with

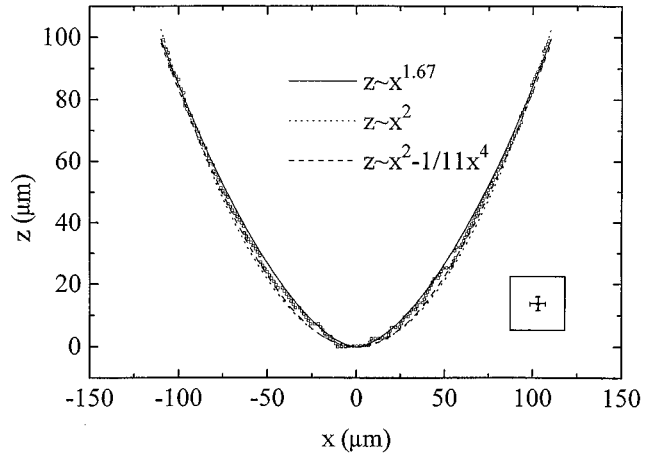


FIG. 6. Data of the contour (\square) of a dendrite very close to the tip ($H < 2R$) are compared with a power-law fit, a parabolic fit, and a parabolic fit with an additional correction term due to anisotropy. All three fits match the contour within experimental error and it cannot be distinguished between the three fits. The error bar in the inset shows the average error of $\pm 4 \mu\text{m}$ of the contour points.

the prediction that close to the tip the shape remains parabolic, but because of the limited resolution of our images, we are not able to distinguish between the three fits (Fig. 6) and it cannot be decided whether the shape is really parabolic or if the power-law fit is valid up to the very tip point.

The prefactor a characterizes the tip just like the tip radius R , but the prefactor a can be determined with much higher precision than R , as the determination of the prefactor a is not restricted to a limited region of the dendrite as it is the case for R . Therefore, we use the prefactor a instead of R in the discussion about tip oscillations. However, for comparison with theories we had to use the more traditional tip radius R .

For the determination of the prefactor, we used $z = a|x|^\beta$ with $\beta = 1.67$ fixed. Fitting both parameters β and the prefactor a simultaneously is not possible as they are coupled nonlinearly, which makes the fit very sensitive to the errors in the data points and the fit becomes unstable. In Fig. 7 the prefactor a is plotted vs the dimensionless supercooling Δ . If z and x are measured in units of R , the prefactor is dimensionless and we find that $a = 0.58 \pm 0.04$ is constant independent of supercooling. This experimental result is again in agreement with the theoretical predictions of Brener and Temkin [29], where a dimensionless prefactor of order unity is predicted, independent of supercooling and anisotropy in the limit of small anisotropy.

B. Tip oscillations

Tip splitting and dynamical tip oscillations have been proposed as the origin of sidebranching (see Sec. IIE). If such tip oscillations exist, oscillations in the tip velocity v_{tip} and in the tip radius R during growth have to be expected. In order to decide whether sidebranches are initiated by oscillatory growth, we have determined time sequences of the prefactor $a(t)$ and the tip velocity v_{tip} during times comparable to the time it takes the tip of the dendrite to grow by about $100R$.

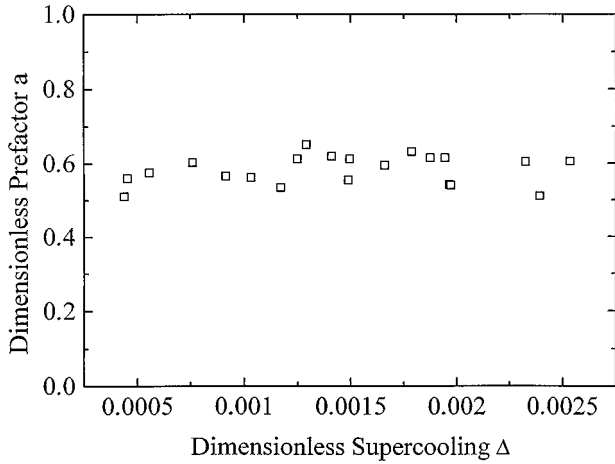


FIG. 7. Dimensionless prefactor a vs the dimensionless supercooling Δ . a is independent of supercooling. The mean value is $a = 0.58 \pm 0.04$.

For the determination of the prefactor $a(t)$, only the tip region of the growing dendrite, i.e., the region without side-branches close to the tip, was imaged on the chip of a CCD camera that was moved with a constant calibrated velocity to follow the dendrite tip. The image field of our optics is much larger than the size of the CCD chip. High optical magnification was chosen to provide the resolution of $1 \mu\text{m}$ on the video pictures. In regular intervals images of the growing dendrite were digitized and the contour of the tip was extracted from each image. In the next step the extracted contour was transformed by a rotation and a translation in such a way that the tip point coincided with the origin and the fourfold symmetry axis of the dendrite was oriented along the z axis of the frame of reference (Fig. 2). After the transformation, the power law $z = a(t)|x|^\beta$, with $\beta = 1.67$, was fitted to the contour to determine the prefactor $a(t)$. Figure 8 shows the prefactor $a(t)$ vs time for a dendrite grown at a supercooling of $\Delta T = 116.3$ mK. We have performed this procedure for long measuring times with a sampling interval of 2 s. Data for short time scales with a sampling interval of

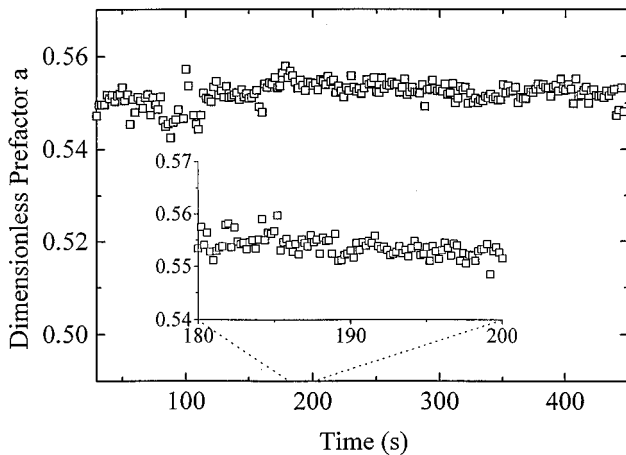


FIG. 8. Dimensionless prefactor a vs time for a dendrite grown at $\Delta T = 116.3$ mK. The sampling interval is 2 s for the large plot and 0.2 s for the smaller inset plot.

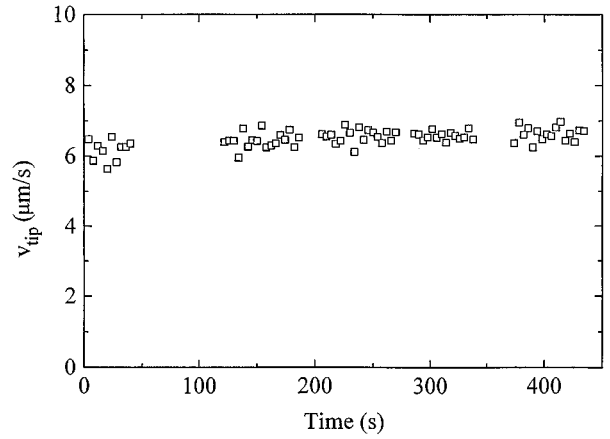


FIG. 9. Instantaneous tip velocity v_{tip} vs time for a dendrite grown at $\Delta T = 141.6$ mK. $v_{\text{tip}} = 6.48 \pm 0.18 \mu\text{m/s}$ is constant in time, indicating stable growth.

0.2 s are shown in the smaller inset plot in Fig. 8. In both cases the prefactor $a(t)$ is constant in time within the precision of our measurements ($\pm 2\%$), showing no oscillatory behavior. Therefore, no tip oscillations can be observed on a time scale ranging from 0.2 s to several minutes. The mean value of the data in the plot is $a = 0.552 \pm 0.002$.

To check our results we have performed the same measurements but used the tip radius R instead of the prefactor a for the characterization of the tip. A sixth-order polynomial was used to determine $R(t)$. Again we find that $R(t)$ is constant in time within $\pm 3\%$. The larger error of $R(t)$ is a consequence of the fact that the prefactor $a(t)$ can be determined with a higher precision than $R(t)$.

The measurement of $v_{\text{tip}}(t)$ was performed in a slightly different way compared to the measurement of $a(t)$. A moving camera would have interfered with the velocity measurements. Therefore, the CCD camera was held fixed in the laboratory frame of reference and the velocity of the dendrite was measured, while the dendrite grew through the field of view of the camera. However, a camera with a fixed position has a drawback. When the dendrite tip is about to leave the field of view of the CCD camera, the camera has to be moved to reposition the dendrite tip in the center of the image. During repositioning of the camera, no tip velocity measurements can be performed. A parabola with a fitting height $H = 2R$ was fitted to the tip to determine the coordinates of the tip point. A parabola fit is sufficient as in the very tip region no noticeable difference to the other fits is found. The sampling rate is limited by the spatial resolution of the CCD camera, i.e. the minimum time between two successive images is given by the time it takes the dendrite to move across one pixel. The tip velocity v_{tip} was determined by measuring the displacement of the tip over time intervals where the tip grows about $10 \mu\text{m}$. Shorter time intervals would lead to significant statistical errors in v_{tip} . In Fig. 9 v_{tip} vs time is plotted for a dendrite grown at a supercooling of 141.6 mK. The tip velocity is constant in time within $\pm 3\%$, indicating stable growth. The mean value is $v_{\text{tip}} = 6.48 \pm 0.18 \mu\text{m/s}$. The gaps in the data points in Fig. 9 are due to the periodic repositioning of the camera.

We conclude that xenon dendrites grow in a stable mode. The dendrite tip does not show any indication of an oscillation.

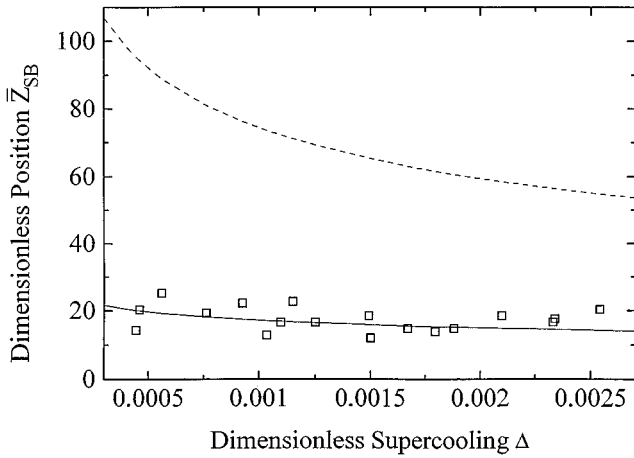


FIG. 10. Position of the first sidebranch \bar{z}_{SB} in units of R vs the dimensionless supercooling Δ . \bar{z}_{SB} is constant and the mean value is $\bar{z}_{\text{SB}} = 18 \pm 3$. The dashed line shows \bar{z}_{SB} according to the theory of Langer, Eq. (40). The solid line shows \bar{z}_{SB} as expected from the theory of Brener, Eq. (41).

tory behavior in the prefactor a or v_{tip} within the precision of our measurements. Therefore, tip oscillations can be excluded as the origin of sidebranching.

C. Sidebranching

A possibility to test whether sidebranching is driven by selective amplification of thermal noise is to measure the mean distance between the tip and the position where the sidebranches have a root-mean-square amplitude $\langle \xi_1(z)^2 \rangle^{1/2}$ of about $1R$ (Fig. 2; see Sec. II E). This mean distance \bar{z}_{SB} for a specific dendrite was obtained by extracting several contours of the dendrite at different growth times and by averaging the positions of all contours. We measured the mean distance \bar{z}_{SB} at various supercoolings in the range $20 \text{ mK} \leq \Delta T \leq 150 \text{ mK}$. Figure 10 shows the position of the first sidebranch \bar{z}_{SB} in units of R as measured in our experiments with xenon dendrites vs the dimensionless supercooling Δ . \bar{z}_{SB} does not depend on supercooling and the mean value is $\bar{z}_{\text{SB}} = 17.5 \pm 3$. We compare these data with theoretical predictions of (i) Langer and (ii) Brener.

(i) Following the theory of Langer, the position of the first sidebranch is given by Eq. (23) for an axisymmetric dendrite. For small Péclet numbers ($p \ll 1$), the dimensionless noise strength \bar{S} introduced in Sec. II E can be written in the form [28]

$$\bar{S} = \left(\frac{T}{T_0} \right) \sigma^{*3/2} p, \quad (37)$$

where

$$T_0 = \left(\frac{L^2 d_0^3}{k_B c_l} \right)^{1/2}. \quad (38)$$

All parameters in Eqs. (37) and (38) are experimentally known and can be used to calculate \bar{z}_{SB} . Using Table I we obtain $T = T_m = 161 \text{ K}$ and $T_0 = 151 \text{ K}$. Moreover, the stability constant $\sigma^* \approx 0.02$ and the Péclet number

$$p = (7.4 \pm 1.4) \times 10^{-1} \Delta^{1.060 \pm 0.028} \quad (39)$$

were measured in previous experiments with xenon dendrites [3,7]. The only undetermined value is the constant \bar{C} . The theoretical value of \bar{C} is of order unity. We set $\bar{C} = 1$ and obtain from Eq. (23)

$$\bar{z}_{\text{SB}} \approx 0.00228 |\ln(0.0022\Delta^{1.06})|^4 \quad (40)$$

for the position of the first sidebranch as a function of the supercooling. In Fig. 10 the dashed line shows \bar{z}_{SB} calculated according to Eq. (40). The mean value of \bar{z}_{SB} of about 70 is much too large, i.e., the growth rate of the sidebranches predicted by the Langer is much too small to explain the experimentally observed sidebranching ($\bar{z}_{\text{SB}} = 18$) and we would have to set $\bar{C} \sim 50$ to find agreement with the experiment. However, setting $\bar{C} \sim 50$ is not permissible as \bar{C} is assumed to be of order unity. The result, that the growth rate predicted by Eq. (40) is much too small to explain the observed sidebranching, is in agreement with an earlier estimate of Langer [28]. Langer mentions that values of \bar{C} in the range $10^1 - 10^2$ would be necessary to make it consistent with experimental data of succinonitrile. Langer concluded that thermal fluctuations are not strong enough to produce the sidebranches.

(ii) However, for a nonaxisymmetric dendrite the amplification rate can be much larger. As mentioned in Sec. II E, Brener and Temkin [23] have found that the amplitude of fluctuations grows exponentially as a function of $(|z|^{2/5}/\sigma^{*1/2})$, which is much faster than the growth of the amplitude of fluctuations as it is expected from the axisymmetric theory of Langer [28], namely, exponentially as a function of $(|z|^{1/4}/\sigma^{*1/2})$. The important point is that in the theory of Brener, the amplification rate is calculated for a nonaxisymmetric dendrite with four fins and a contour of the fins of $z = a|x|^{5/3}$. As xenon dendrites do have exactly this kind of shape (Sec. IV A), this theory seems well applicable to the case of three-dimensional xenon dendrites.

Using Eq. (25) for the position of the first sidebranch in the nonaxisymmetric case, with the same values and the same fluctuation strength as above and $\bar{C} = 1$, we obtain

$$\bar{z}_{\text{SB}} \approx 0.0261 |\ln(0.0022\Delta^{1.06})|^{5/2} \quad (41)$$

for the position of the first sidebranch as a function of supercooling. As can be seen in Fig. 10 (solid line), we find good agreement between this calculation and our data within experimental error. The dependence of \bar{z}_{SB} on supercooling, as predicted by the above-mentioned theories of Langer and Brener, cannot be verified with our data because our measurement of the position of the first sidebranch is not precise enough.

Our measurement of \bar{z}_{SB} shows quantitative agreement with the analytic work of Brener and Temkin [29] for a nonaxisymmetric dendrite with cubic symmetry. Therefore we conclude that thermal noise initiates the formation of sidebranches.

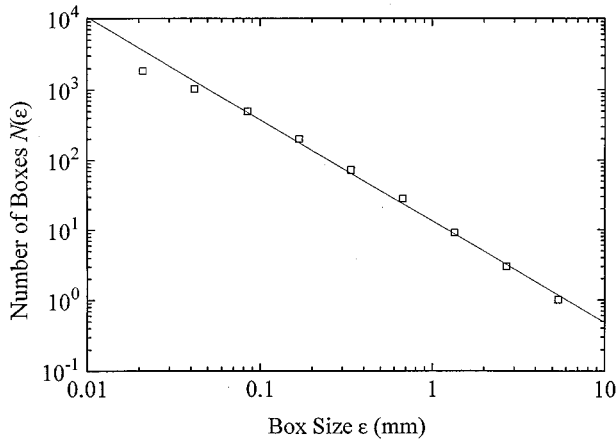


FIG. 11. Number of “boxes” $N(\epsilon)$ vs the length scale ϵ of the boxes. The slope of the linear fit is -1.44 ± 0.03 .

D. Fractal dimension

We determined the fractal dimension of the contour of the area of projection of a xenon dendrite [51]. In the first step, the contour of the dendrite was extracted from a digitized image and afterward box counting was used to calculate the fractal dimension. To simplify the algorithm the contour was covered with a square mesh of side ϵ , where ϵ was chosen to be $\epsilon = 2^n \times (\text{pixel size})$, with $n = 0, \dots, 9$ for a 512×512 pixel image. Figure 11 shows $\ln N(\epsilon)$ plotted versus $\ln \epsilon$ for a xenon dendrite grown at a supercooling of $\Delta T = 61.1$ mK.

The data points can be approximated by a straight line and the slope of the linear fit is -1.44 ± 0.03 with a correlation coefficient of 0.998. The data point for the smallest box size ϵ has been ignored in the fit, as ϵ is of order of the tip radius R for this data point, which is at the theoretical limit of the scaling range. Although the linear fit is not perfect, we find that the contour is fractal over a range of more than two orders of magnitude in length scale and more than three orders of magnitude in the number of “boxes” scale. The fractal dimension is $d_f \approx 1.4$ according to Eq. (28). The scaling range is limited at the lower end by the radius of curvature, which is the typical length of the smallest structures of a dendrite, and at the upper end by the overall size of the dendrite.

To verify our results we also used the correlation method developed by Grassberger and Procaccia (Sec. IIF). Figure 12 shows a plot of $\ln C(r)$ versus $\ln r$. $C(r)$ has been calculated for the contour of a xenon dendrite. The data points are on a straight line, which means again that the contour is fractal over a range of more than two orders of magnitude in length scale. The slope of the linear fit corresponds to the “correlation dimension” $\nu = 1.488 \pm 0.004$. The correlation coefficient of the linear fit is 0.9996. The fact that both methods lead, within the errors of the data, to the same results strongly indicates that the contour is indeed fractal over a range of more than two orders of magnitude in length scale. Using both methods, we have calculated the fractal dimension at different times during the growth of a xenon dendrite. We find that after a short transient time at the beginning, when the dendrite starts growing out of the capillary, the fractal dimension is constant in time, i.e., there is no time dependence of the fractal dimension during growth. To mini-

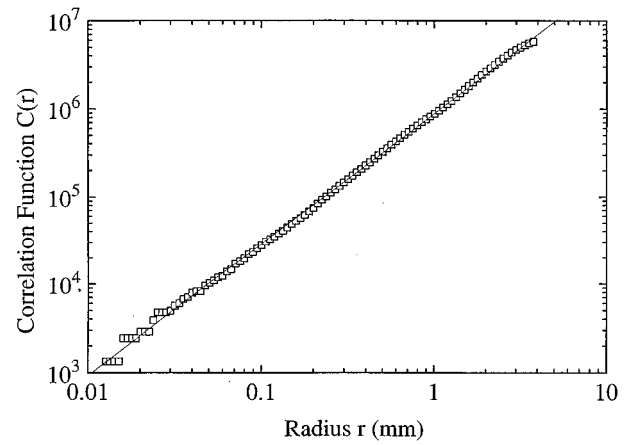


FIG. 12. Correlation function $C(r)$ vs the length scale r . The slope of the linear fit is $\nu = 1.488 \pm 0.004$.

mize the statistical errors, we calculated the fractal dimension at several “ages” of a specific dendrite and then averaged in order to get the averaged fractal dimensions \bar{d}_f and $\bar{\nu}$ for a given supercooling. Figure 13 shows \bar{d}_f and $\bar{\nu}$ calculated for various supercoolings. The results of both methods are shown together.

From these experimental results we conclude that the fractal dimension does not depend on supercooling. Both methods lead to the same results within the errors of the data. However, the correlation method seems to give systematically slightly higher values. We do not understand why this happens. Theory would require $\bar{\nu} \leq \bar{d}_f$. We suppose that this disagreement might be an effect of a systematic error in the algorithm. Averaging over data obtained at various supercoolings leads to $\bar{d}_f = 1.42 \pm 0.05$ (box dimension) and $\bar{\nu} = 1.51 \pm 0.08$ (correlation dimension). The dendrites can be considered to be self-similar. At a given temperature the length scale is changed in all dimensions in the same way. Dendrites grown at various temperatures are self-similar; they scale with R .

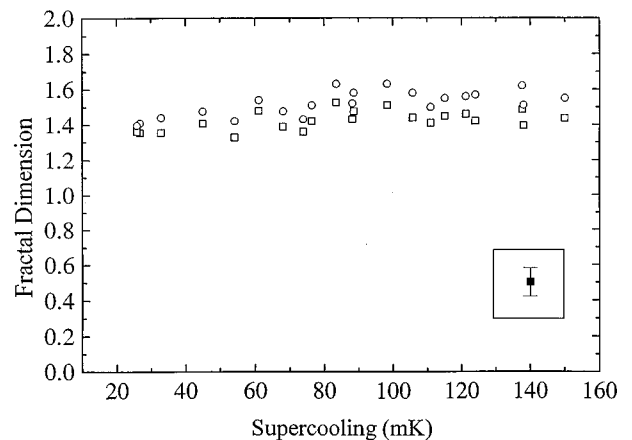


FIG. 13. Averaged box dimension $\bar{d}_f = 1.42 \pm 0.05$ (\square) and the averaged correlation dimension $\bar{\nu} = 1.51 \pm 0.08$ (\circ) vs the supercooling of the melt. The error bar in the inset shows the average error of the data points.

V. DISCUSSION

A. Tip shape

Up to now most theoretical studies on dendritic growth assume an axisymmetric, parabolic tip of the dendrite, based on the famous Ivantsov solution [13]. However, it is known from experiments [3,7,8] since many years that the tip shape deviates from a parabola, but it was commonly assumed that this deviation may be neglected. Our results show that the deviation from a parabolic shape is significant and that it is essential to take into account the nonparabolic, nonaxisymmetric tip shape to understand three-dimensional dendritic growth.

La Combe *et al.* [9] investigated the tip region of pure, three-dimensional succinonitrile dendrites. Using a parabola fit, a dependence of the tip radius R on the fitting height H was found, similar to the one reported by Hürlimann *et al.* [7]. It was concluded that this dependence is due to the nonparabolic shape of the tip and a fourth-order polynomial was used for a more accurate determination of the tip radius.

In contrast to La Combe *et al.*, we find that the shape of the dendrite tip cannot be approximated accurately by a low-order polynomial and we use a power-law fit instead. The power-law fit matches the contour within the resolution of our data ($\pm 1 \mu\text{m}$) and there is no dependence of the fit on the fitting height H . Highly contrasted images with high resolution were used to extract the contour of the tip. Therefore, we conclude that the contour of the fins has the shape $z = a|x|^\beta$, with $a = 0.58 \pm 0.04$ and $\beta = 1.67 \pm 0.05$. The values a and β have been predicted by Brener and Temkin [29] and therefore the physical meanings of these parameters are known, whereas in the case of a polynomial fit of degree n , the physical meanings of the $(n+1)$ fitting parameters are unknown.

However, the problem with a nonparabolic dendrite tip is that the tip radius is not a well-defined quantity anymore. For a tip with a power-law shape with $\beta \neq 2$, the curvature, and therefore the tip radius R , becomes singular at the tip point ($x=0$). This is a serious problem as the tip radius is the important length scale in dendritic growth. The prefactor a used in the previous sections, which was made dimensionless by measuring all lengths in units of R , cannot be used to define a length. We propose to use the unscaled and temperature-dependent prefactor $\tilde{a}(\Delta)$ to define a new length R_a , which might be used in place of the traditional tip radius R . $\tilde{a}(\Delta)$ has the dimension of $(\text{length})^{-2/3}$. R_a can be defined as

$$R_a(\Delta) = \tilde{a}(\Delta)^{-3/2}, \quad (42)$$

R_a and R are of the same order of magnitude and have the same temperature dependence. The similarity between R and R_a is a consequence of the fact that the dimensionless prefactor a is constant and independent of supercooling (Sec. IV A) if all lengths are scaled by the tip radius $R(\Delta)$. The notation $R(\Delta)$ indicates that the tip radius depends on supercooling. The shape of the contour in the tip region can be written as [see Eq. (18)]

$$\left(\frac{\tilde{z}}{R(\Delta)}\right) = a \left(\frac{\tilde{x}}{R(\Delta)}\right)^{5/3}, \quad (43)$$

where \tilde{x} and \tilde{z} are the unscaled coordinates as measured in the experiment. A simple rearrangement leads to

$$\tilde{z} = a \left(\frac{R}{R^{5/3}}\right) \tilde{x}^{5/3} \quad (44)$$

and the unscaled prefactor $\tilde{a}(\Delta)$ is given to be

$$\tilde{a}(\Delta) = a R^{-2/3}. \quad (45)$$

This leads to

$$R_a(\Delta) = \tilde{a}(\Delta)^{-3/2} = a^{-3/2} R(\Delta) \quad (46)$$

for the scaling behavior of $R_a(\Delta)$. Therefore, R_a and R provide the same physical information and are related by the proportionality constant $a^{-3/2} \approx 2.4$, independent of supercooling.

B. Sidebranching

We find quantitative agreement of our experimental data of \bar{z}_{SB} with the theoretical predictions of Brener and Temkin [29]. As far as we know, the theory of Brener and Temkin [29] is the first analytic treatment of a nonaxisymmetric dendrite in three dimensions for a material with cubic symmetry. This theory describes the formation of four fins along the dendrite, as observed in our experiments with xenon dendrites.

In a further test of the theory of Brener and Temkin one might compare the predictions of \bar{z}_{SB} with experimental results obtained from dendrites grown from other substances to check whether the theory predicts the dependence of \bar{z}_{SB} of the material properties and noise strength in the right way. To perform a comparison with the theory of Brener and Temkin similar to the one with xenon dendrites, we used the experimental data for three-dimensional succinonitrile dendrites obtained by La Combe *et al.* [9]. We estimate from Fig. 7 of Ref. [9] that the position where the first sidebranches have a root-mean-square amplitude of $1R$ is about $300 \mu\text{m}$. The dendrite was grown at a supercooling of 0.46 K . At this supercooling, the tip radius is $25.7 \mu\text{m}$ and we get $\bar{z}_{\text{SB}} = 11.5 \pm 3$. With the properties of succinonitrile $T_m = 331 \text{ K}$, $T_0 = 1280 \text{ K}$, $\bar{C} = 1$, $\sigma \sim 0.02$, and $p = 5 \times 10^{-3}$ and using Eq. (25), we obtain $\bar{z}_{\text{SB}} = 14.5$ for the position of the first sidebranch measured in units of R . This is compatible with the theory of Brener. We cannot perform a quantitative comparison between experiment and theory as we did it for xenon because we have only one single data point for succinonitrile and our estimate of \bar{z}_{SB} is not very precise. Although succinonitrile and xenon have rather different material properties, Brener's theory describes correctly the sidebranching behavior for both substances. This result suggests that Brener's theory describes correctly the sidebranching behavior of dendrites for any pure substance with cubic symmetry.

C. Fractal dimension

The result that sidebranching is initiated by thermal noise is consistent with the observation that sidebranches on opposite sides of the dendrite are not correlated. The spatial Fourier transform of the shape of the dendrite has a broad con-

tinuous background, which is typical for a dynamical chaotic system. Integral parameters, such as the fractal dimension, have proven to be useful for the characterization of such dynamical, chaotic systems.

The value 1.4 for the fractal dimension of xenon dendrites is not compatible with the fractal dimension $d_f=1.71$, which is found in two-dimensional, isotropic DLA. The reason for this discrepancy may be that two-dimensional, isotropic DLA is too simplistic to describe three-dimensional dendritic solidification. The fractal dimension of 1.4 is in approximate agreement with the two-dimensional simulations of dendritic growth of Nittmann and Stanley [36] (Sec. IIF), which predict a fractal dimension of 1.5, and the two-dimensional, anisotropic DLA simulations of Arneodo *et al.* [37], which predict a fractal dimension of $d_f=3/2$ for dendritic growth patterns. However, these results should not be overestimated as in these simulations two-dimensional volume fractals are calculated, whereas in the case of xenon dendrites we studied the contour of the projection of a three-dimensional dendrite and it is not clear how the contour is related to the two-dimensional volume. Our results are in agreement with the predictions of the phase diagram proposed by Brener, Müller-Krumbhaar, and Temkin [34] (Sec. IIF) for the selection of growth patterns in diffusional growth. They predict fractal growth patterns for crystals with small anisotropy growing at small supercoolings. This is in agreement with xenon dendrites that are found to be fractal. Xenon has only a small anisotropy, as it is a very simple, monoatomic substance with van der Waals forces only. Furthermore, all xenon dendrites in our experiments are grown at very small supercoolings. Larger supercoolings are not possible because of heterogeneous nucleation of crystals at the walls of the growth vessel. Therefore, it is not possible to verify the predicted crossover [34] from fractal structures at small supercoolings to seaweedlike structures at larger supercoolings.

VI. SUMMARY

Anisotropic surface properties lead for the xenon dendrites to a nonaxisymmetric shape with fourfold symmetry. Four fins grow along the main stem of the dendrite, starting immediately behind the tip. The contour of these fins is not parabolic and can be described by a power law $z=a|x|^\beta$, with $a=0.58\pm 0.04$ and $\beta=1.67\pm 0.05$ independent of supercooling. This result is in excellent agreement with the analytical work of Brener *et al.* [22,23,29], which predicts a

contour of $z\sim|x|^{5/3}$ for a three-dimensional nonaxisymmetric dendrite with cubic symmetry. Only very near the tip ($H<2R$) the contour can be approximated by a parabola fit and for $H\rightarrow 0$ the experimental data are in agreement with $v_{\text{tip}}R^2=\text{const.}$

We have determined the tip velocity $v_{\text{tip}}(t)$ and the dimensionless prefactor $a(t)$ as a function of time. In both cases $v_{\text{tip}}(t)$ and the prefactor $a(t)$ are constant in time, showing no oscillatory behavior within the resolution of experimental data. The dendrite grows in a stable mode. Thus tip oscillations can be excluded from being the origin of sidebranching. Our determination of the position of the first sidebranch \bar{z}_{SB} shows quantitative agreement with the analytic work of Brener Temkin [29] for a nonaxisymmetric dendrite with cubic symmetry. Therefore we conclude that thermal noise initiates the formation of sidebranches.

Further away from the dendrite tip, where the sidebranches are becoming larger, many fewer theories and experimental data are available. In this region nonlinear interactions among different sidebranches are important and coarsening takes place. We find that integral parameters such as the volume, the surface area, and the contour length of the projection, which were determined in earlier measurements with xenon dendrites [7], are good parameters to describe the whole dendrite. The fractal dimension is another integral parameter. We find that the contour of a xenon dendrite is fractal over more than two orders of magnitude of length scale and has a fractal dimension $\bar{d}_f=1.42\pm 0.05$. Both box counting and correlation method lead to the same results within the errors of the data. \bar{d}_f is independent of supercooling. The fact that xenon dendrites are fractal is in agreement with the predictions of the phase diagram of Brener *et al.* [34] for the selection of growth patterns in diffusional growth, where fractal growth patterns are predicted for crystals with small anisotropy grown at small supercoolings. Thus we conclude that integral parameters are good parameters for the characterization of dendritic solidification. It may be that integral parameters can be used in other structure-forming phenomena.

ACKNOWLEDGMENTS

Our gratitude goes to our colleagues and collaborators. We thank Dr. H.R. Ott for his support. This work was supported by the Swiss National Science Foundation.

-
- [1] W. Kurz and D.J. Fisher, *Fundamentals of Solidification*, 3rd ed. (Trans Tech., Aedermannsdorf, 1989).
 - [2] J.S. Langer, in *Chance and Matter*, Proceedings of the Les Houches Summer School of Theoretical Physics, Session XLVI, Les Houches, 1986, edited by J. Souletie, J. Vannimenus, and R. Stora (North-Holland, Amsterdam, 1987), p. 629.
 - [3] J.H. Bilgram, M. Firmann, and E. Hürlimann, *J. Cryst. Growth* **96**, 175 (1989).
 - [4] S.-C. Huang and M. Glicksman, *Acta Metall.* **29**, 717 (1981).
 - [5] R. Trivedi and J.T. Mason, *Metall. Trans. A* **22**, 235 (1991).
 - [6] Y. Pomeau and M. Ben Amar, in *Solids far from Equilibrium*, edited by C. Godrèche (Cambridge University Press, Cambridge, 1992), p. 365.
 - [7] E. Hürlimann, R. Trittbach, U. Bisang, and J.H. Bilgram, *Phys. Rev. A* **46**, 6579 (1992).
 - [8] A. Dougherty and J.P. Gollub, *Phys. Rev. A* **38**, 3043 (1988).
 - [9] J.C. LaCombe, M.B. Koss, V.E. Fradkov, and M.E. Glicksman, *Phys. Rev. E* **52**, 2778 (1995).
 - [10] J.P. Hansen and I.R. McDonald, *Theory of Simple Liquids* (Academic, London, 1976).
 - [11] J.S. Langer, *Rev. Mod. Phys.* **52**, 1 (1980).

- [12] A. Papapetrou, *Z. Krist.* **92**, 89 (1935).
- [13] G.P. Ivantsov, *Dokl. Akad. Nauk SSSR* **58**, 567 (1947).
- [14] G.P. Ivantsov, in *Growth of Crystals*, edited by A.V. Shubnikov and N.N. Sheftal (Consultants Bureau, New York, 1958), Vol. I, p. 76.
- [15] J.S. Langer and H. Müller-Krumbhaar, *Acta Metall.* **26**, 1681 (1978).
- [16] M.E. Glicksman, R.J. Schaefer, and J.D. Ayers, *Metall. Trans. A* **7**, 1747 (1976).
- [17] E.R. Rubinstein and M.E. Glicksman, *J. Cryst. Growth* **112**, 84 (1991); **112**, 97 (1991); A. Dougherty, *ibid.* **110**, 501 (1991); M.E. Glicksman and N.B. Singh, *ibid.* **98**, 277 (1989).
- [18] D.A. Kessler, J. Koplik, and H. Levine, *Adv. Phys.* **37**, 255 (1988).
- [19] C. Misbah, H. Müller-Krumbhaar, and Y. Saito, *J. Cryst. Growth* **99**, 150 (1990).
- [20] M. Muschol, D. Liu, and H.Z. Cummins, *Phys. Rev. A* **46**, 1038 (1992).
- [21] D.A. Kessler and H. Levine, *Acta Metall.* **36**, 2693 (1988).
- [22] M. Ben Amar and E. Brener, *Phys. Rev. Lett.* **71**, 589 (1993).
- [23] E. Brener, *Phys. Rev. Lett.* **71**, 3653 (1993).
- [24] W.W. Mullins and R.F. Sekerka, *J. Appl. Phys.* **35**, 444 (1964).
- [25] O. Martin and N. Goldenfeld, *Phys. Rev. A* **35**, 1382 (1987).
- [26] H. Honjo and S. Ohta, *J. Cryst. Growth* **131**, 111 (1993).
- [27] R. Pieters and J.S. Langer, *Phys. Rev. Lett.* **56**, 1948 (1986).
- [28] J.S. Langer, *Phys. Rev. A* **36**, 3350 (1987).
- [29] E. Brener and D.E. Temkin, *Phys. Rev. E* **51**, 351 (1995).
- [30] E. Brener and D.E. Temkin, *Pis'ma Zh. Éksp. Teor. Fiz.* **59**, 697 (1994) [*JETP Lett.* **59**, 738 (1994)].
- [31] J. Feder, *Fractals* (Plenum, New York, 1988); S.H. Strogatz, *Nonlinear Dynamics and Chaos* (Addison-Wesley, Reading, MA, 1994); P. Bergé, Y. Pomeau, and C. Vidal, *Order within Chaos* (Wiley, New York, 1986).
- [32] P. Grassberger and I. Procaccia, *Phys. Rev. Lett.* **50**, 346 (1983).
- [33] D. Ruelle, *Proc. R. Soc. London Ser. A* **427**, 241 (1990).
- [34] E. Brener, H. Müller-Krumbhaar, and D. Temkin, *Europhys. Lett.* **17**, 535 (1992).
- [35] H.E. Stanley, *Physica A* **186**, 1 (1992).
- [36] J. Nittmann and H.E. Stanley, *J. Phys. A* **20**, L981 (1987).
- [37] A. Arneodo, F. Argoul, Y. Couder, and M. Rabaud, *Phys. Rev. Lett.* **66**, 2332 (1991).
- [38] R.C. Brower, D.A. Kessler, J. Koplik, and H. Levine, *Phys. Rev. Lett.* **51**, 1111 (1983).
- [39] E. Ben-Jacob, N.D. Goldenfeld, J.S. Langer, and G. Schön, *Phys. Rev. A* **29**, 330 (1984).
- [40] B. Caroli, C. Caroli, B. Roulet, and J.S. Langer, *Phys. Rev. A* **33**, 442 (1986); D.I. Meiron, *ibid.* **33**, 2704 (1986); A. Barbieri, D.C. Hong, and J.S. Langer, *ibid.* **35**, 1802 (1986); D.A. Kessler, J. Koplik, and H. Levine, *ibid.* **33**, 3352 (1986).
- [41] Y. Saito, G. Goldbeck-Wood, and H. Müller-Krumbhaar, *Phys. Rev. Lett.* **58**, 1541 (1987).
- [42] R. Kobayashi, *Exp. Math.* **3**, 59 (1994).
- [43] J. Maurer, B. Perrin, and P. Tabeling, *Europhys. Lett.* **14**, 575 (1991).
- [44] J.H. Hollomon and D. Turnbull, in *Progress in Metal Physics*, edited by B. Chalmers (Pergamon, London, 1953), Vol. IV, p. 357.
- [45] R.E. Bedford, G. Bonnier, H. Maas, and F. Parsec, *Metrologia* **20**, 145 (1984).
- [46] Instruction manual to the Linde rare-gas purifier M1.
- [47] Visilog, *A Tutorial on Image Processing* (Noesis, Jouy en Josas, 1991).
- [48] R. Bucher, Eidgenössische Technische Hochschule Diploma thesis, Zürich, 1993 (unpublished).
- [49] U. Bisang and J.H. Bilgram, *J. Cryst. Growth* (to be published).
- [50] U. Bisang and J.H. Bilgram, *Phys. Rev. Lett.* **75**, 3898 (1995).
- [51] U. Bisang and J.H. Bilgram, *J. Cryst. Growth* (to be published).
- [52] J. Ancsin, *Metrologia* **14**, 45 (1978).
- [53] *Rare Gas Solids*, edited by M.L. Klein and I.A. Venables (Academic, New York, 1977).
- [54] *Selected Values of the Thermodynamic Properties of the Elements* (American Society for Metals, Metals Park, OH, 1973).
- [55] *Thermophysical Properties of Matter* (Plenum, New York, 1970), Vol. 3.
- [56] W. M. Yen and R. E. Norberg, *Phys. Rev.* **131**, 269 (1963).
- [57] A. C. Sinnock and B. L. Smith, *Phys. Rev.* **181**, 1297 (1969).